

## Subannual variability of the ocean circulation in the Kuroshio region

Maurice J. Schmeits<sup>1</sup> and Henk A. Dijkstra

Institute for Marine and Atmospheric Research Utrecht, Utrecht University, Utrecht, Netherlands

Received 24 July 2001; revised 3 July 2002; accepted 15 August 2002; published 31 December 2002.

[1] Using altimeter data of the Kuroshio region, dominant patterns of variability are determined by applying multichannel singular spectrum analysis. A statistically significant propagating mode of variability with a timescale close to 7 months is found. In addition, output from a high-resolution simulation of the Parallel Ocean Climate Model (POCM) is analyzed, which also displays variability on a timescale of 7 months, although not statistically significant at the 95% confidence level. To explain the physics of the apparent preference for variability at this timescale within a strongly eddying flow, we investigate the stability of barotropic North Pacific flows. Within a shallow-water model, there appear to be three different steady flow paths of the Kuroshio that all become unstable to oscillatory modes. One of these modes has a timescale of 7 months for reasonable values of the parameters and has other features in common with the 7-month statistical modes from the POCM output and from the observations. The connection between results from the stability analysis and from the analysis of the observations and POCM output leads to the conjecture that the preference for the 7-month variability is due to the existence of a large-scale barotropic instability of the mean Kuroshio path. *INDEX TERMS:* 3220 Mathematical Geophysics: Nonlinear dynamics; 4255 Oceanography: General: Numerical modeling; 4576 Oceanography: Physical: Western boundary currents; *KEYWORDS:* Kuroshio, variability, observations, models, bifurcation

**Citation:** Schmeits, M. J., and H. A. Dijkstra, Subannual variability of the ocean circulation in the Kuroshio region, *J. Geophys. Res.*, 107(C12), 3235, doi:10.1029/2001JC001073, 2002.

### 1. Introduction

[2] The most intense current in the North Pacific Ocean is the Kuroshio. Its time mean path is now quite well known. From observations, it is found that the Kuroshio path exhibits bimodal behavior to the south of Japan with transitions occurring between a small and a large meander state [Taft, 1972]. Both states can persist over a period ranging from a few years to a decade and transitions between them occur within a couple of months [Kawabe, 1986]. The mean zonal geostrophic transport of the Kuroshio is estimated to be about 52 Sv ( $\text{Sv} \equiv 10^6 \text{ m}^3 \text{ s}^{-1}$ ) at 137°E [Qiu and Joyce, 1992]. At the southeast corner of Honshu, the Kuroshio separates from the Japanese coast and flows eastward, while meandering increases. However, the current keeps a mean latitudinal position of about 35°N up to 180°E.

[3] Like the Gulf Stream, the Kuroshio transports enormous amounts of heat northward, although its thermohaline component is much weaker and consequently its northward extent is much less. The mean Kuroshio position, as well as its variability is therefore relevant to the climate system. Similar to the 9-month variability in the Gulf Stream region

[Lee and Cornillon, 1995; Schmeits and Dijkstra, 2000], near-annual variability is also found in recent studies of the Kuroshio Extension. Wang *et al.* [1998] have used four years of data from the TOPEX/Poseidon (T/P) exact repeat mission (ERM) together with 2.3-year data from the Geosat ERM. They have separated the low-frequency variability into subannual, annual and interannual variability through filtering processes. Hövmöller diagrams (their Figures 9 and 14) show that the subannual sea level height fluctuations are primarily propagating westward and they weaken away from the Kuroshio axis (at about 35°N). The dominant complex empirical orthogonal functions (CEOFs) have an average period of about 9 months, but the spatial structure differs between the CEOFs. The authors speculate that instability and/or external forcing might be responsible for the generation of the subannual variability and that bottom topography plays a role as well.

[4] Using both ECMWF atmospheric fields and Geosat data, Kelly *et al.* [1996] also found variability with time-scales of 5–9 months in both the Gulf Stream and the Kuroshio. For both western boundary currents, they found correlations between the height difference across the jet (surface transport) and the path itself. This suggests that there are structural changes in the recirculation gyres, associated with a path change. Although wind stress (curl) is clearly correlated with surface transport, mean path and net surface heat flux in both ocean basins, there is no clear correlation between net surface heat flux and surface trans-

<sup>1</sup>Now at Royal Netherlands Meteorological Institute (KNMI), de Bilt, Netherlands.

port over the entire study region. They concluded that, at least in the North Atlantic, the structural changes in the recirculation gyres may not be related to surface heat flux variations.

[5] Both Kuroshio and Gulf Stream are western boundary currents with strong mesoscale activity [Hall, 1991]. This variability is dominated by eddies, arising mainly through baroclinic instability, that have typical timescales of 2–3 months [Adamec, 1998] and spatial scales on the order of the internal Rossby deformation radius. Modeling studies [Smith *et al.*, 2000] and observational studies [Cronin and Watts, 1996] have indicated that the eddies have a strong effect on the time mean flow and have to be well resolved to obtain a correct mean path of the Gulf Stream. In such a strongly nonlinear flow, it is remarkable that there appears to be a preference for subannual variability (9 months) [Schmeits and Dijkstra, 2000].

[6] Because of the dynamical similarity between the Kuroshio and the Gulf Stream, it is expected that such a preference for specific subannual timescales occurs in the Kuroshio as well. Following the same approach as Schmeits and Dijkstra [2000], multivariate time series analysis techniques are used to extract statistically significant modes of variability in T/P-ERS sea surface height (SSH) observations of the Kuroshio region. Indeed, a preferred propagating spatial pattern is found, with a timescale close to 7 months. This timescale of variability is also found in the output from a simulation of the Parallel Ocean Climate Model (POCM) [Semtner and Chervin, 1992; Stammer *et al.*, 1996], that is analyzed with the same statistical techniques (section 2).

[7] To identify the origin of the preference for the 7-month timescale, the stability of the barotropic North Pacific wind-driven circulation is studied within a shallow-water model with realistic geometry and forcing (section 3). In the discussion (section 4), we connect the results from the observations, from the POCM output and from the stability analysis to argue that a particular barotropic instability is likely to contribute to the preference for the 7-month timescale.

## 2. Data Analysis

### 2.1. Data Sets and Their Preprocessing

[8] The data sets used in this study are maps of sea level anomalies from the combined TOPEX/Poseidon and ERS-2 missions (T/P-ERS) and output from a particular simulation of POCM. The T/P-ERS data set consists of interpolated altimeter data, that are corrected for all geophysical, media and instrument effects as well as for orbit error (ERS only). For more information on the data processing, the error estimation, and the gridding procedure the reader is referred to Le Traon *et al.* [1998]. The T/P-ERS SSH anomalies have a spatial resolution of  $\frac{1}{4}^\circ \times \frac{1}{4}^\circ$  and a temporal resolution of 10 days. For the analysis of T/P-ERS SSH we use data in the Kuroshio region ( $25^\circ$ – $44^\circ$ N,  $120^\circ$ E– $170^\circ$ W) from April 1995 to July 1999.

[9] The basic POCM formulation has been described by Semtner and Chervin [1992] and Stammer *et al.* [1996]. The POCM output analyzed is from run 4C having an average horizontal resolution of  $\frac{1}{4}^\circ$  and 20 nonequidistant levels in the vertical direction. The global simulation was performed

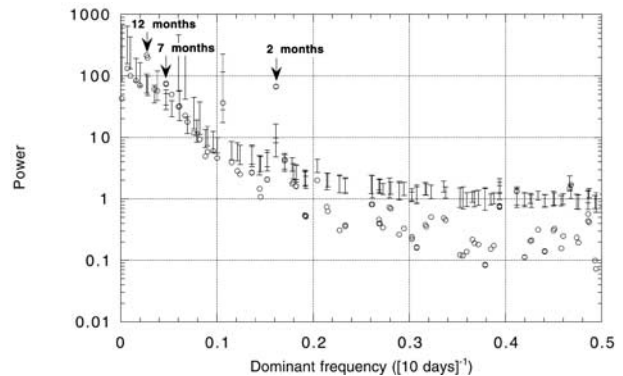


**Figure 1.** Monte Carlo significance test of T/P-ERS SSH data in the Kuroshio region for the period April 1995 to July 1999, using  $L = 24$  PCs from a conventional PCA as the input channels. Shown are projections of the SSH data onto the data adaptive basis, with a 50-month window ( $M = 50$ ). Open circles show the data eigenvalues, plotted against the dominant frequency of the corresponding ST-PC. The vertical bars show the 95% confidence interval computed from 1000 realizations of a noise model consisting of  $L$  independent AR(1) processes with the same variance and lag-1 autocorrelation as the input data channels.

over the period 1979–1998 and the ocean was forced by either ECMWF reanalysis (1979–1993) or ECMWF operational (1994–1998) fields of heat fluxes, freshwater fluxes, and wind stress. These fields are updated every 3 days and interpolated to the time step. The annual river outflow was also included in the freshwater flux. Diffusion is handled using a biharmonic closure for both momentum and tracers [Stammer *et al.*, 1996]. For more details about this simulation the reader is referred to <http://vislab-www.nps.navy.mil/~rtt>. We have used monthly mean temperature fields at three depth levels, namely 160 m (T160), 310 m (T310) and 610 m (T610) in the Kuroshio region ( $25^\circ$ – $50^\circ$ N,  $120^\circ$ – $180^\circ$ E) from 1979 to 1998. SSH is a prognostic variable in POCM because of the incorporation of a free surface formulation.

[10] The seasonal cycle has been eliminated from the POCM output by computing anomalies about the 1979–1998 monthly climatology. In this way, effects of the seasonal atmospheric forcing have been removed from the POCM output. Note that the seasonal cycle has not been eliminated from the T/P-ERS data set, because the time period is too short (about 4 years) to yield a robust monthly climatology. Both data sets have been prefiltered with principal component analysis (PCA) [Preisendorfer, 1988] in order to reduce the number of spatial degrees of freedom in the data sets. Finally, the statistical mean at each point has been removed prior to the analysis. The multivariate data are then analyzed with the aid of multichannel singular spectrum analysis (M-SSA) [Plaut and Vautard, 1994; Allen and Robertson, 1996], of which the basics are shown in Appendix A.

### 2.2. Spatiotemporal Variability of T/P-ERS SSH Observations

[11] The T/P-ERS SSH anomalies were prefiltered with standard PCA and the leading 24 PCs, which account for 76% of the variance, provide the  $L$  input channels for the

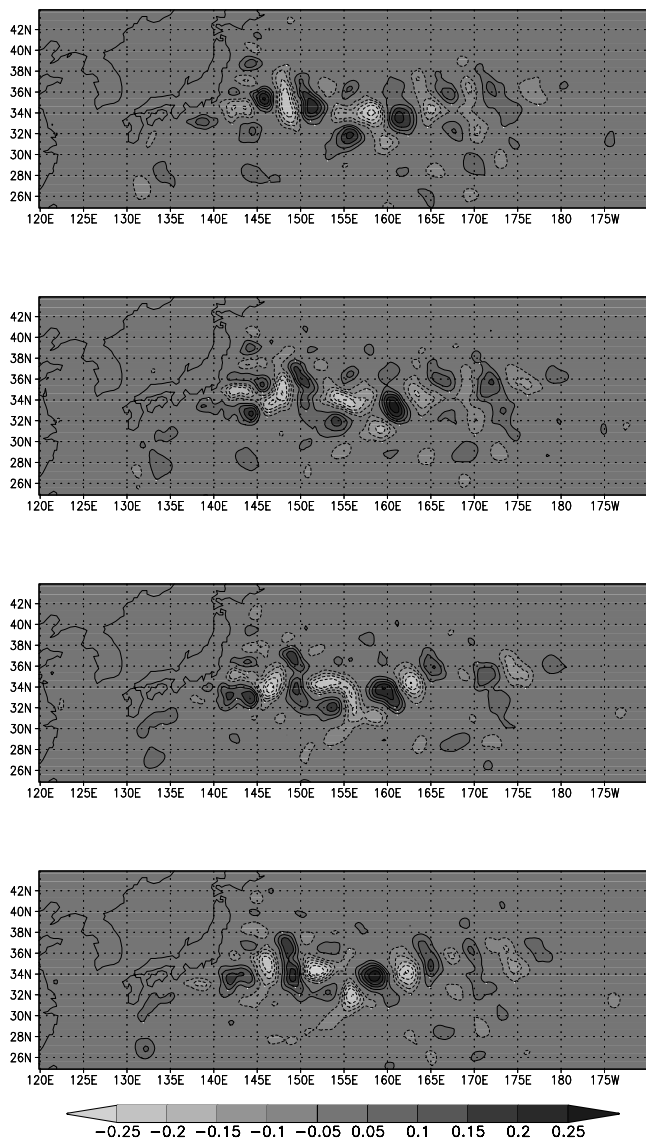


**Figure 2.** Reconstructed component (RC) pair 6–7 of Kuroshio SSH (m) describing the oscillatory statistical mode having a 7-month timescale. The patterns are shown at a monthly interval, starting in mid-September 1997, over about one half cycle of the oscillation; the other half cycle is similar but with anomalies of reversed sign.

M-SSA algorithm. We have more than 4 years of data ( $N = 158$ ), and use a standard window length of 500 days ( $M = 50$ ).

[12] The result of the Monte Carlo significance test for M-SSA (Appendix A) is shown for the data adaptive basis in Figure 1. Three data eigenvalue pairs, with associated periods of 12, 7, and 2 months, are indicated as significant. Because the seasonal cycle has not been removed from the T/P-ERS data set (subsection 2.1), the signature of the steric response to the seasonal heating cycle shows up as the dominant ST-PC pair, explaining 26% of the variance in the 24 leading PCs. The 7-month timescale belongs to ST-PC pair 6–7 (Figure 1), which explains 9% of the variance in the 24 leading PCs. ST-PC 6 and 7 are in quadrature, which suggests that the pair represents an oscillatory statistical

mode with a dominant period of 7 months. We have checked the robustness of this 7-month statistical mode with respect to a different value of the window length of 400 days ( $M = 40$ ). For this value of  $M$ , the 7-month timescale is also indicated as significant by the Monte Carlo test for M-SSA (not shown). Finally, the 2-month timescale is related to mesoscale variability over the domain, very likely due to baroclinic eddies, with also a large amplitude west of Japan. Our focus will be on the 7-month variability and both the patterns of the 2-month and the 12-month variability are not further discussed.

[13] Figure 2 represents the anomaly patterns of Reconstructed Components (RC; see Appendix A) 6–7 for four phases during the oscillation. The starting time was chosen to be September 1997, when the amplitude of the statistical mode is quite large, and each subsequent picture is 1 month later. Together, the pictures show nearly half of the cycle of the oscillation and the other half cycle is similar but with anomalies of reversed sign. The anomalies are concentrated around the mean axis of the Kuroshio Extension and their maximum amplitude is 31 cm. In Figure 3, we show the propagating SSH anomalies associated with this RC pair along 35°N. A series of positive and negative anomalies propagates westward, that is, upstream, with an average velocity of about  $3 \text{ cm s}^{-1}$ . The zonal wavelength associated with this RC pair is on the order of  $6^\circ$ , which corresponds to 546 km at  $35^\circ\text{N}$ . At  $35^\circ\text{N}$  the continental

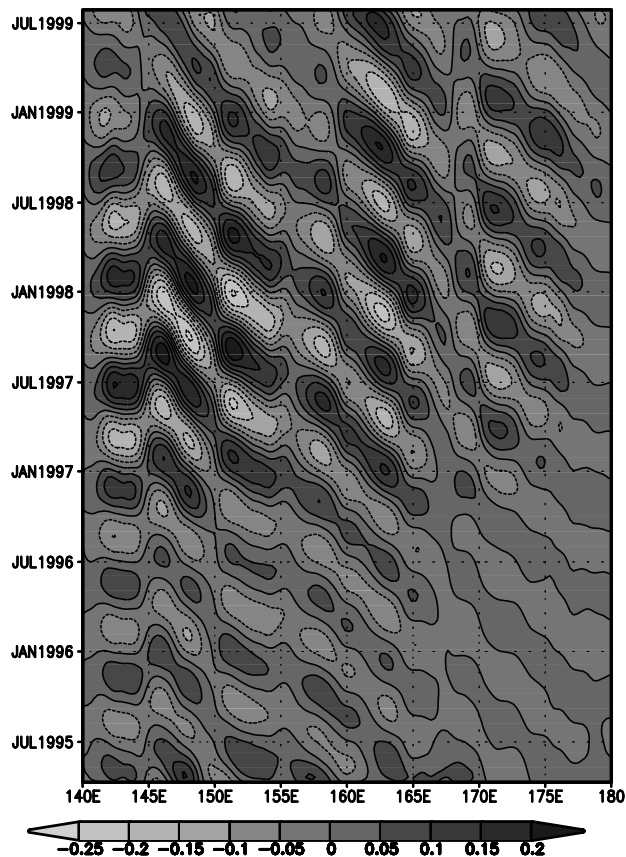


**Figure 3.** RC pair 6–7 of Kuroshio SSH (m) describing the oscillatory statistical mode having a 7-month timescale. The anomalies are shown along  $35^\circ\text{N}$  as a function of longitude and time.

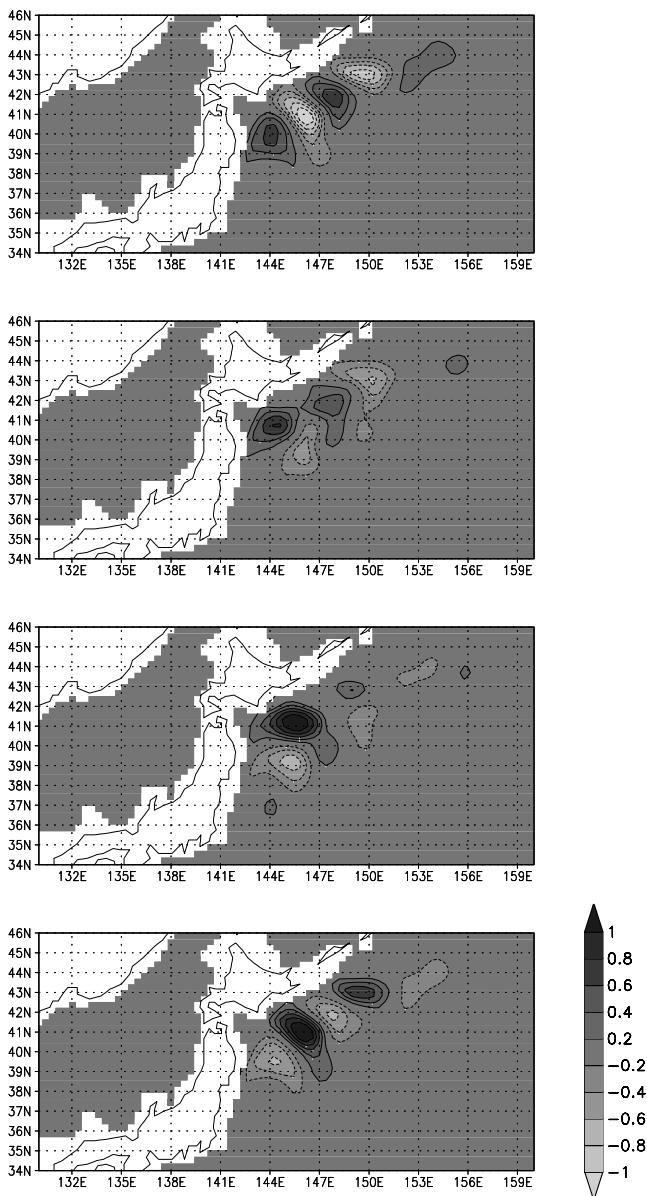


**Figure 4.** RC pair 3–4 of high-pass filtered Kuroshio T310 (K) from POCM describing the oscillatory statistical mode having a 7-month timescale. The patterns are shown at a monthly interval, starting in January 1984, over one half cycle of the oscillation; the other half cycle is similar but with anomalies of reversed sign.

rise is situated between about  $140^{\circ}$  and  $143^{\circ}$ E, and there seems to be interaction of the mode with this bottom topographic feature (Figure 3). No clear interaction is visible, however, with the other major bottom topographic features in the Kuroshio Extension region, namely the Shatsky Rise and Hess Rise. Although the 7-month variability of the Kuroshio has a clear signature at the surface, its vertical structure is unknown. Therefore, we investigate in the next subsection whether there is evidence of such 7-month variability in subsurface layers of POCM.

### 2.3. Spatiotemporal Variability of POCM Fields

[14] For POCM, we have analyzed simulated temperature fields at three depth levels, namely 160 m (T160), 310 m (T310)

and 610 m (T610). The analysis has been performed for each field separately, and in all cases described below, the nonseasonal anomalies were prefiltered with standard PCA. The leading PCs, which account for 70% or more of the variance, provide the  $L$  input channels for the M-SSA algorithm. Since we have obtained 20 years of data, the value of  $N = 240$ .

[15] First, we report results from the M-SSA analyses of unfiltered T160 ( $L = 17$ ), T310 ( $L = 14$ ) and T610 ( $L = 12$ ) using a window length  $M$  of 80 months. In all data sets there is an oscillatory mode of variability with a timescale of 7 months, which is nearly statistically significant at the 95% confidence level. However, because the M-SSA analysis of

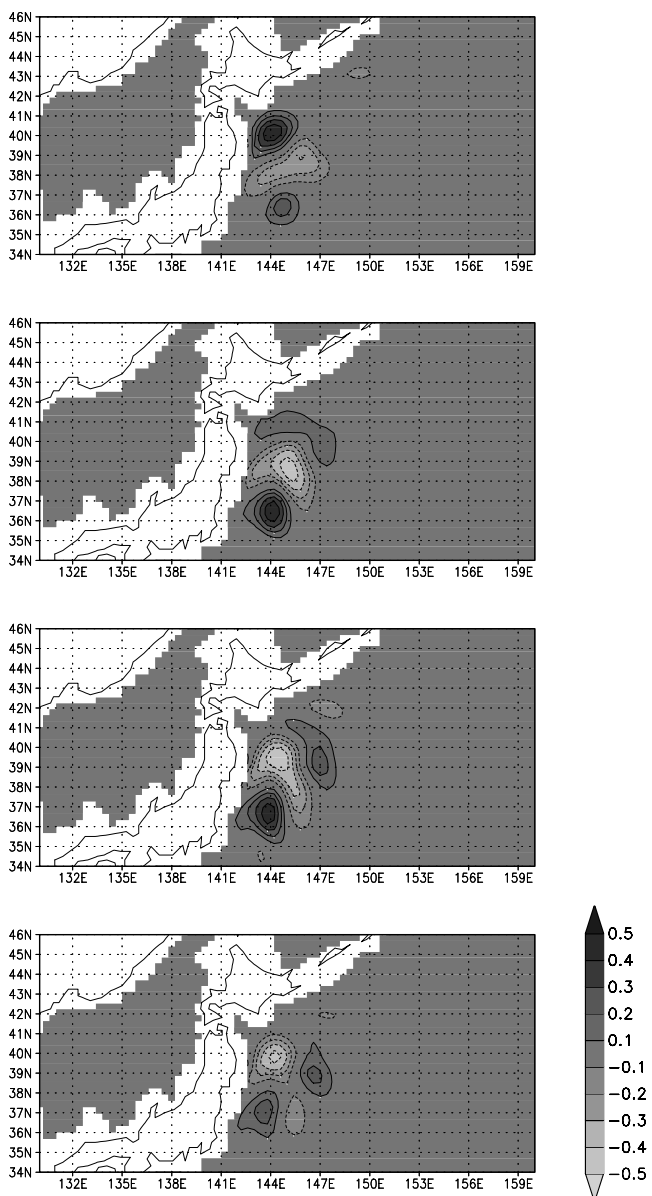


**Figure 5.** RC pair 7–8 of high-pass filtered Kuroshio T610 (K) from POCM describing the oscillatory statistical mode having a 7-month timescale. The patterns are shown at a monthly interval, starting in January 1984, over one half cycle of the oscillation; the other half cycle is similar but with anomalies of reversed sign.

T/P-ERS data indicated the 7-month timescale as statistically significant, and we are interested in the vertical structure of the 7-month mode, the reconstructed anomaly patterns of T160, T310 and T610 for this mode were computed after having filtered the data sets. As the eigenvalues corresponding to the 7-month mode in the unfiltered data sets have low rank orders, the nonseasonal T160, T310 and T610 anomalies were filtered using a high-pass filter in order to remove timescales longer than 9 months. For the filtered data sets, a window length  $M$  of 9 months was used.

[16] For the filtered T160 ( $L = 38$ ), T310 ( $L = 35$ ) and T610 ( $L = 28$ ) data sets, the 7-month timescale belongs to a ST-PC pair that is in quadrature, which suggests that the pair represents an oscillatory statistical mode. The reconstructed anomaly patterns of T310 for this mode are shown in Figure 4 for four phases during the oscillation. The starting time was chosen to be January 1984, when the amplitude of the statistical mode is quite large, and each subsequent picture is 1 month later; together the pictures show nearly half of the cycle of the oscillation. The anomalies are rotating in the Kuroshio separation region of POCM, contrary to the anomalies associated with the 7-month statistical mode from the T/P-ERS altimeter data, which are also present in the Kuroshio Extension region (Figure 2). However, there are also corresponding features: the anomalies of both statistical modes are concentrated around the mean axis of the Kuroshio and they have a wavelength in the same order of magnitude (around 500 km).

[17] The anomalies associated with the 7-month statistical mode from the POCM output have a maximum amplitude of 2.3 K for T160, 2.2 K for T310, and 1.0 K for T610. The spatial patterns of the 7-month statistical mode in T160 and T310 are very similar and hence the former are not shown. The reconstructed anomaly patterns of T610 for this mode are shown in Figure 5 for four phases during the oscillation, with again a starting time in January 1984. Although the areas of large amplitude have shifted slightly southward with respect to those in T310 (see Figure 4), some vertical coherence of the signal in the first upper 600 m can be distinguished. Near 40°N, the temperature anomalies have the same sign at all three depths. To see this coherence in more detail, the time series of the mode at different depth levels at the location (144°E, 40°N) are plotted in Figure 6. For more than half of the time, the curves are in phase.

### 3. Stability of Barotropic North Pacific Flows

#### 3.1. Formulation

[18] Consider a flat-bottomed ocean basin with a realistic horizontal domain,  $\mathcal{V}$ , and bounded by a closed contour  $\Gamma$ . The density of the ocean is constant and the flow is driven by a climatological wind stress  $\tau(\phi, \theta) = \tau_0(\tau^\phi, \tau^\theta)$ , where  $\tau_0$  is the amplitude and  $(\tau^\phi, \tau^\theta)$  provides the spatial pattern [Trenberth *et al.*, 1989]. Lateral friction, with lateral friction coefficient  $A_H$ , is the dissipative mechanism in the model. In the usual notation, the velocities in eastward and northward directions are indicated by  $u$  and  $v$ , respectively and  $h$  is the thickness of the water column (with equilibrium value  $D$ ), and changes due to changes in the SSH. The governing shallow-water equations are nondimensionalized using scales  $r_0$ ,  $D$ ,  $U$ ,  $r_0/U$  and  $\tau_0$  for length, layer depth, velocity,

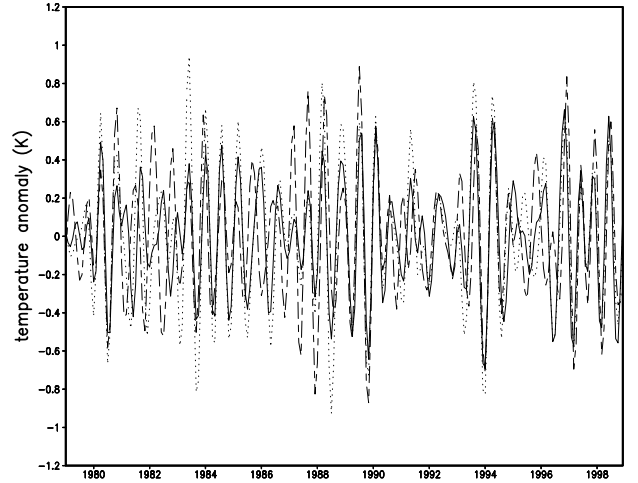


**Figure 6.** RCs of high-pass filtered Kuroshio T160 (solid), T310 (dotted), and T610 (dashed) from POCM describing the oscillatory statistical mode having a 7-month timescale. The time series are shown at (144°E, 40°N).

time, and wind stress, respectively, where  $r_0$  is the radius of the earth, and become

$$\epsilon \left( \frac{\partial u}{\partial t} + \frac{u}{\cos \theta} \frac{\partial u}{\partial \phi} + v \frac{\partial u}{\partial \theta} - uv \tan \theta \right) - v \sin \theta = -\frac{\epsilon F}{\cos \theta} \frac{\partial h}{\partial \phi} + E \left( \nabla^2 u - \frac{u}{\cos^2 \theta} - \frac{2 \sin \theta}{\cos^2 \theta} \frac{\partial v}{\partial \phi} \right) + \alpha \frac{\tau^\phi}{h} \quad (1a)$$

$$\epsilon \left( \frac{\partial v}{\partial t} + \frac{u}{\cos \theta} \frac{\partial v}{\partial \phi} + v \frac{\partial v}{\partial \theta} + u^2 \tan \theta \right) + u \sin \theta = -\epsilon F \frac{\partial h}{\partial \theta} + E \left( \nabla^2 v - \frac{v}{\cos^2 \theta} + \frac{2 \sin \theta}{\cos^2 \theta} \frac{\partial u}{\partial \phi} \right) + \alpha \frac{\tau^\theta}{h} \quad (1b)$$

$$\frac{\partial h}{\partial t} + \frac{1}{\cos \theta} \left( \frac{\partial(hu)}{\partial \phi} + \frac{\partial(hv \cos \theta)}{\partial \theta} \right) = 0. \quad (1c)$$

On the boundary  $\Gamma$  of the domain no-slip conditions are prescribed; that is,

$$(\phi, \theta) \in \Gamma : \quad u = v = 0. \quad (2)$$

[19] The parameters in these equations are the Rossby number  $\epsilon$ , the Froude number  $F$ , the Ekman number  $E$ , and the wind stress coefficient  $\alpha$ . Expressions for these parameters are

$$\epsilon = \frac{U}{2\Omega r_0}; \quad F = \frac{gD}{U^2}; \quad E = \frac{A_H}{2\Omega r_0^2}; \quad \alpha = \frac{\tau_0}{2\Omega \rho D U}, \quad (3)$$

where  $\Omega$  is the angular velocity of the earth. Standard values of the parameters in this model are listed in Table 1.

#### 3.2. Implementation

[20] Within the SW model, a finite difference discretization was used on a staggered grid on the domain [120°E, 150°W]  $\times$  [10,55]°N with a resolution of  $\frac{5^\circ}{12} \times \frac{5^\circ}{12}$ . We have

**Table 1.** Standard Values of Parameters in the Barotropic SW Model

Parameter		Value
<i>Dimensional Parameters</i>		
$r_0$		$6.37 \times 10^6$ m
$D$		$1.0 \times 10^3$ m
$g$		$9.8$ ms <sup>-2</sup>
$\rho$		$1.0 \times 10^3$ kg m <sup>-3</sup>
$\tau_0$		$1.3 \times 10^{-1}$ Pa
$A_H$		$2.0 \times 10^2$ m <sup>2</sup> s <sup>-1</sup>
$U$		$1.0 \times 10^{-1}$ ms <sup>-1</sup>
$\Omega$		$7.3 \times 10^{-5}$ s <sup>-1</sup>
<i>Dimensionless Parameters</i>		
$\alpha$		$8.8 \times 10^{-3}$
$\epsilon$		$1.1 \times 10^{-4}$
$E$		$3.4 \times 10^{-8}$
$F$		$9.8 \times 10^5$

taken the 100 m depth contour as the continental boundary because otherwise the modeled Kuroshio would enter the East China Sea. In reality, it is steered by bottom topography, so that it follows a more or less straight path from Taiwan to Japan. Continental geometry and boundary conditions are taken into account by first discretizing the equations on the sphere and then substituting equations with boundary conditions, according to whether the point is a land point or an ocean point. To ensure overall mass conservation, an integral condition for  $h$  over the domain  $\mathcal{V}$  is implemented [Schmeits and Dijkstra, 2000]; that is

$$\int_{\mathcal{V}} h \cos \theta d\phi d\theta = |\mathcal{V}|, \quad (4)$$

where  $|\mathcal{V}|$  is the (dimensionless) area of the domain since the layer depth is scaled with  $D$ .

[21] The basic technique for dynamical systems analysis is comprised of two main pieces: a continuation method to advance one step on a branch of steady states as a parameter is varied, and an eigenvalue solver to determine the linear stability of the computed steady state. The barotropic shallow-water model can be written in operator form as follows

$$\mathcal{M} \frac{\partial \mathbf{u}}{\partial t} + \mathcal{L} \mathbf{u} + \mathcal{N}(\mathbf{u}) = \mathbf{F} \quad (5)$$

where  $\mathcal{L}$ ,  $\mathcal{M}$  are linear operators,  $\mathcal{N}$  is a nonlinear operator,  $\mathbf{u}$  is the vector of dependent quantities and  $\mathbf{F}$  contains the forcing of the system. To determine the steady states  $\bar{\mathbf{u}}$  of the system of equations when parameters are changed, the problem

$$\mathcal{L} \bar{\mathbf{u}} + \mathcal{N}(\bar{\mathbf{u}}) = \mathbf{F} \quad (6)$$

has to be solved.

[22] When a steady state is determined, the linear stability of the solution is considered and transitions that mark qualitative changes such as transitions to multiple equilibria (pitchfork or saddle node bifurcations) or periodic behavior (Hopf bifurcations) can be detected. To determine the linear stability of the steady state, perturbations  $\tilde{\mathbf{u}}$  are considered.

With  $\mathbf{u} = \bar{\mathbf{u}} + \tilde{\mathbf{u}}$ , linearizing (5) around  $\bar{\mathbf{u}}$  and separating  $\tilde{\mathbf{u}} = \hat{\mathbf{u}} e^{\sigma t}$  gives an eigenvalue problem of the form

$$(\mathcal{L} + \mathcal{N}_u) \hat{\mathbf{u}} = -\sigma \mathcal{M} \hat{\mathbf{u}} \quad (7)$$

where  $\mathcal{N}_u$  is the derivative of the operator  $\mathcal{N}$  with respect to  $\mathbf{u}$ . In most applications, discretization of this eigenvalue problem leads to a generalized algebraic eigenvalue problem of the form

$$\mathcal{A} \hat{\mathbf{x}} = \sigma \mathcal{B} \hat{\mathbf{x}} \quad (8)$$

where  $\mathcal{A}$  and  $\mathcal{B}$  are nonsymmetric matrices. Bifurcations are detected from crossings of  $\sigma$  with the imaginary axis. Solution techniques for equations (6)–(8) are presented by Dijkstra [2000].

### 3.3. Results

[23] The bifurcation diagram (Figure 7a) has been computed for steady wind forcing using the Ekman number as a control parameter, the latter being the most uncertain parameter in the model. Every point on a curve in the

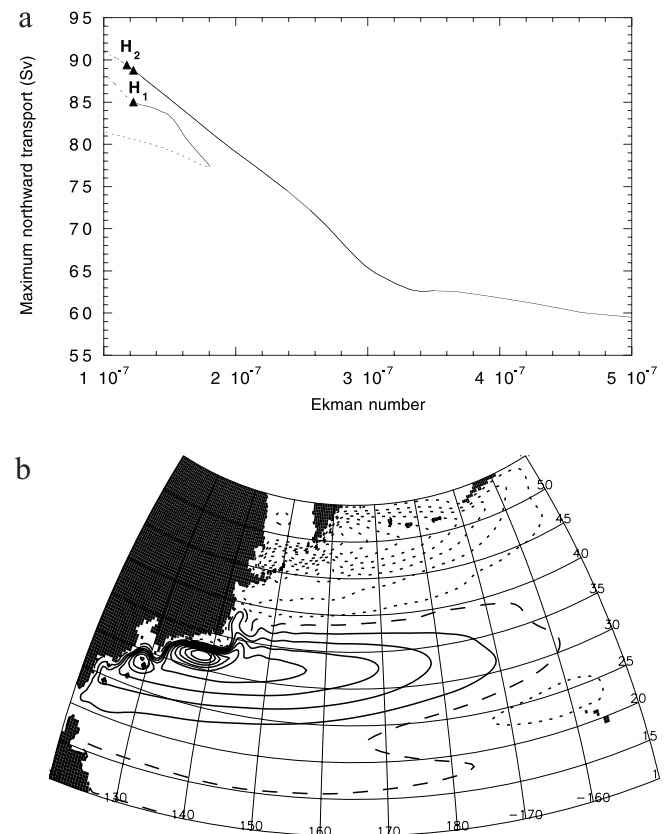


**Figure 7.** (a) Bifurcation diagram for the barotropic shallow-water model on the North Pacific domain with the Ekman number as control parameter. Solid (dotted) branches indicate stable (unstable) steady states, whereas the Hopf bifurcation points are indicated by triangles. (b) Contour plot of SSH deviations for the steady state solution at  $E = 1.5 \times 10^{-7}$  on the upper branch in Figure 7a. The contour levels are scaled with respect to the maximum value of the field.

bifurcation diagram corresponds to a stationary state and stability is indicated with the line style (drawn is stable and dotted is unstable). On the vertical axis, the maximum northward volume transport  $\Phi$  (in Sv) over a section is shown which is calculated as

$$\Phi = (U D r_0) \max \int_{\phi_w}^{\phi} v h \cos \theta d\phi \quad (9)$$

where the maximum is taken both over  $\phi$  and  $\theta$ . All parameters except the Ekman number are fixed as in Table 1. The bifurcation diagram (Figure 7a) consists of a perturbed pitchfork bifurcation [Golubitsky and Schaeffer, 1985] and clearly shows that multiple equilibria exist when the lateral friction is small enough. Schmeits and Dijkstra [2001] have shown that these multiple equilibria are related to the different meandering structures of the Kuroshio. Note that there is quite a range of Ekman numbers where two equilibria are (barotropically) stable. Down to  $E = 1.8 \times 10^{-7}$ , there is a unique steady solution for each value of the Ekman number (Figure 7a).

[24] The upper branch of solutions in Figure 7a continues to exist for values smaller than  $E = 1.8 \times 10^{-7}$ , but the solutions lose stability at  $E = 1.2 \times 10^{-7}$ . They become unstable to one oscillatory mode at a Hopf bifurcation  $H_1$  and to another oscillatory mode at Hopf bifurcation  $H_2$  (Figure 7a). A stable stationary solution on this branch is shown for  $E = 1.5 \times 10^{-7}$  in Figure 7b. Stationary solutions on the lower branch are shown by Schmeits and Dijkstra [2001, Figure 7].

[25] The pattern of an eigenmode is determined from the eigenvector  $\hat{\mathbf{x}} = \hat{\mathbf{x}}_R + i\hat{\mathbf{x}}_I$  associated with the eigenvalue  $\sigma = \sigma_r + i\sigma_i$  in (8). These span an oscillatory mode given by

$$\Xi(t) = e^{\sigma_r t} [\hat{\mathbf{x}}_R \cos(\sigma_i t) - \hat{\mathbf{x}}_I \sin(\sigma_i t)] \quad (10)$$

with dimensional period  $T = 2\pi r_0 / (U\sigma_i)$ . The oscillatory mode that becomes unstable at  $H_1$  has a period of 2 months. It is shown at four phases within half a period of the oscillation in Figures 8a–8d. Its maximum response is found in the high shear region to the south of Kamchatka, the propagation direction is eastward and the perturbations have a typical wavelength of 600 km. The relevance of this dynamical mode to the variability in the northwestern part of the Pacific basin is not further considered.

[26] A second Hopf bifurcation ( $H_2$ ) occurs at  $E = 1.2 \times 10^{-7}$  on the upper branch in Figure 7a. The transition structure of the perturbation is shown in Figures 9a–9d. The dynamical mode is located in the separation region of the Kuroshio and propagates eastward. It has a period of 3 months, and a wavelength of about 550 km. The timescale of this mode turns out to be insensitive to the layer thickness  $D$ , at least for values of  $D$  up to 1200 m.

[27] Another oscillatory mode, which is also located in the separation region of the Kuroshio, has been found on the upper branch in Figure 7a, but it is stable for the standard value of  $D$ . The period of this oscillation is about 5 months. We have investigated the sensitivity of this mode to the layer thickness  $D$ . It turns out that for slightly larger values of  $D$ , the mode becomes unstable, and we denote the associated Hopf bifurcation by  $H_3$ ; for  $D = 1044$  m the

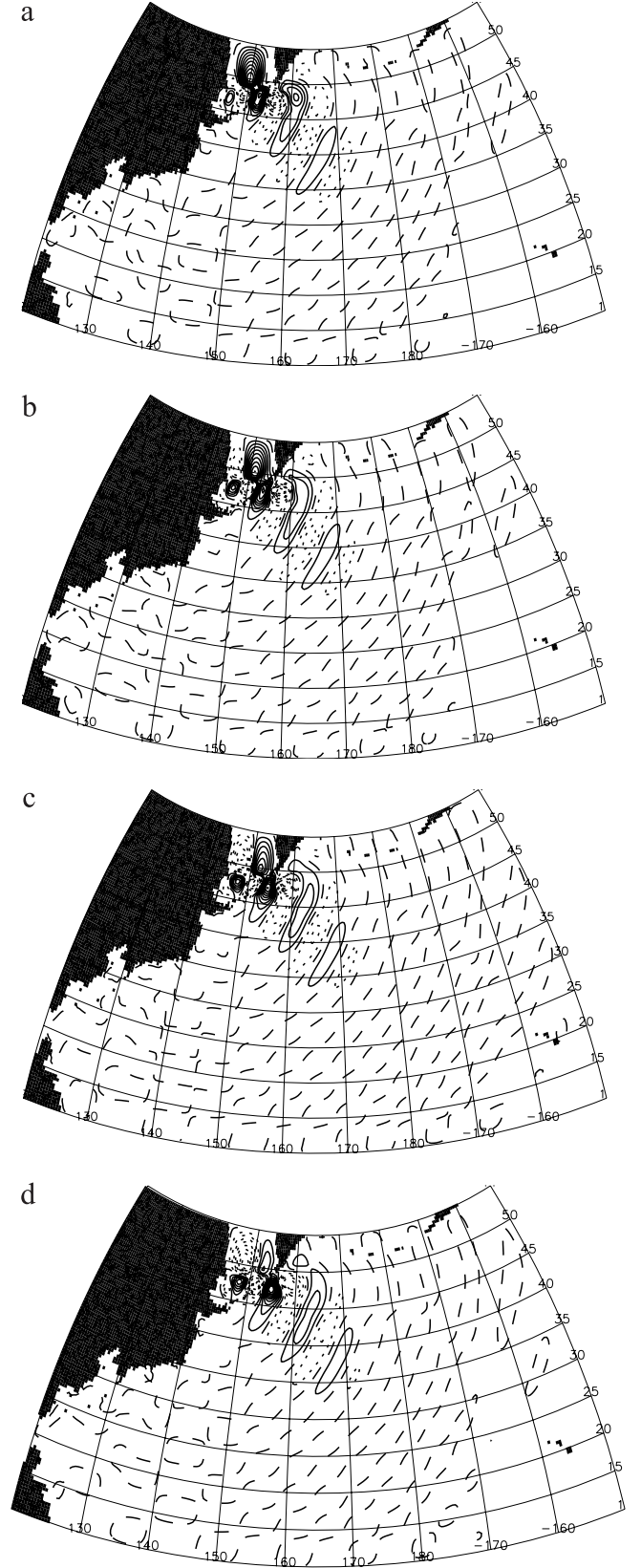


**Figure 8.** Contour plot of the layer thickness anomaly of the transition structure (Figures 8a–8d) of the neutral mode at the Hopf bifurcation  $H_1$  in Figure 7a at several phases of the oscillation: (a)  $\sigma_i t = 0$ , (b)  $\sigma_i t = \pi/4$ , (c)  $\sigma_i t = \pi/2$ , and (d)  $\sigma_i t = 3\pi/4$ .

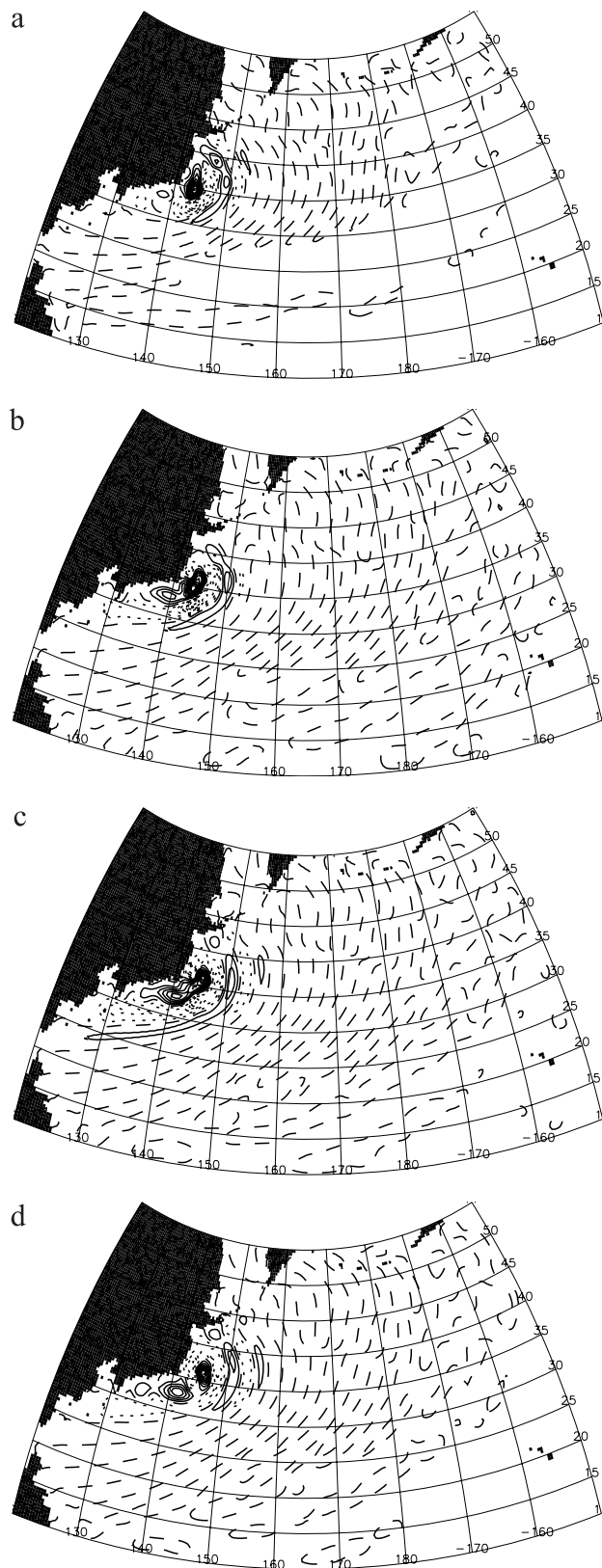


**Figure 9.** Contour plot of the layer thickness anomaly of the transition structure (Figures 9a–9d) of the neutral mode at the Hopf bifurcation  $H_2$  in Figure 7a at several phases of the oscillation: (a)  $\sigma_{it} = 0$ , (b)  $\sigma_{it} = \pi/4$ , (c)  $\sigma_{it} = \pi/2$ , and (d)  $\sigma_{it} = 3\pi/4$ .

Hopf bifurcation  $H_3$  occurs at  $E = 1.1 \times 10^{-7}$ . The transition structure of the perturbation is shown in Figures 10a–10d, with the basic state being similar to that in Figure 7b. The dynamical mode has a period of about 6 months, it propagates westward, that is, upstream and the perturbations have a typical wavelength of 450 km. By adding the perturbation to the steady state, we can see in Figure 11 that the perturbation causes the southern recirculation gyre both to stretch and contract during one period of the oscillation.

[28] For several values of  $D$ , the value of  $E$  is determined at which the Hopf bifurcation  $H_3$  occurs (Figure 12a). The spatial pattern of the neutral mode does not change much with  $D$ , but the period of the oscillation increases from 6 to 8 months in the range of  $D$  considered (Figure 12b). Of course, the average depth of the real Kuroshio separation region is much larger, but the value of  $D$  is restricted because the velocities of the mean state, and hence the horizontal shear, have to be realistic. For  $D = 1000$  m, the order of magnitude of the geostrophic velocities in both the SW-model and POCM is the same. Moreover, as the wind does not influence the circulation in the deeper ocean, values slightly larger than 1 km do seem to be reasonable. Inclusion of bottom topography could change the barotropic mode and its period substantially, but it was not considered here.

#### 4. Summary and Discussion

[29] From M-SSA analysis of T/P-ERS SSH observations in the Kuroshio region, a mode of variability with a timescale of 7 months and a zonal length scale of about 550 km has been found. Based on the Monte-Carlo significance test for M-SSA [Allen and Robertson, 1996], it follows that this type of variability is very unlikely to be caused by red noise processes [Hasselmann, 1976]. The anomalies are concentrated around the mean axis of the Kuroshio Extension (Figure 2) and they are propagating westward, that is, upstream (Figure 3). These features of the subannual variability in the Kuroshio region are in correspondence with the results in the study of Wang *et al.* [1998], although they found a somewhat longer timescale (9 months). With the fact that a similar timescale of variability (5–9 months) has also been found in another study [Kelly *et al.*, 1996], we conclude that there is preferred variability on a 7-month timescale in the Kuroshio region.

[30] M-SSA analysis of POCM temperature fields also shows variability on a timescale of 7 months. The spatial pattern of the anomalies is centered around the mean axis of the Kuroshio and the anomalies have a spatial scale of about 400–500 km. Contrary to the results from observations, the anomalies associated with the 7-month statistical mode from the POCM output are concentrated in the Kuroshio separation region and amplitudes are small in the Kuroshio Extension. Hence, although the same timescale and length scales are found, the spatial patterns of variability are substantially different.

[31] In this paper, we have identified a possible explanation for the preferred variability on the 7-month timescale as being due to a large-scale barotropic instability of the time mean flow. Analysis of the stability of steady barotropic wind-driven flows in the North Pacific basin reveals

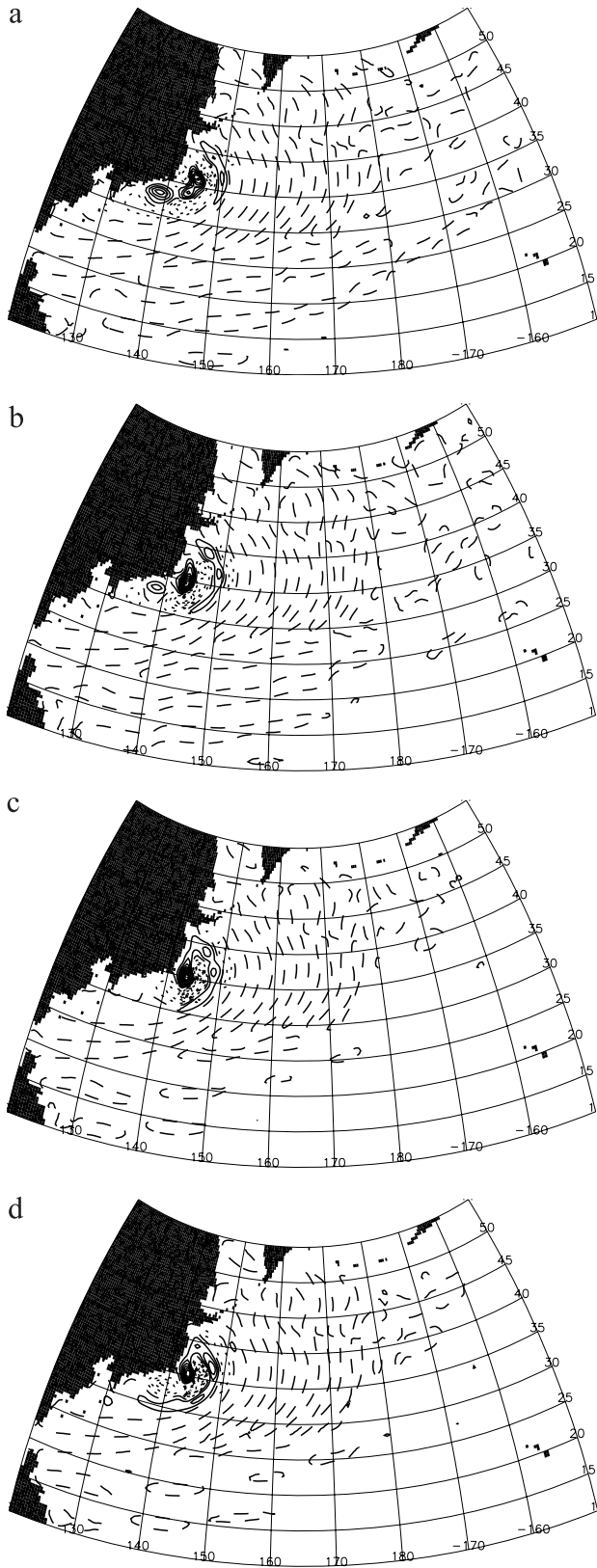


**Figure 10.** Contour plot of the layer thickness anomaly of the transition structure (Figures 10a–10d) of the neutral mode at the Hopf bifurcation  $H_3$  for  $D = 1044$  m (see also Figure 12a) at several phases of the oscillation: (a)  $\sigma_{it} = 0$ , (b)  $\sigma_{it} = \pi/4$ , (c)  $\sigma_{it} = \pi/2$ , and (d)  $\sigma_{it} = 3\pi/4$ .

that unstable oscillatory dynamical modes exist with sub-annual timescales. For an average depth of the basin of 1100 m (Figure 12b), one of these modes has a timescale of 7 months. Its perturbation pattern is localized in the separation region of the Kuroshio, with very small amplitude over the remainder of the basin (Figure 10), and it causes the southern recirculation gyre both to stretch and contract during one period of the oscillation (Figure 11). As *Schmeits and Dijkstra* [2000] did, we will refer to this dynamical mode as the barotropic western boundary current (BWBC) mode. In other studies, using a hierarchy of models of the wind-driven circulation, it is found that these barotropic oscillatory modes are robust modes of variability [*Dijkstra*, 2000; *Nauw and Dijkstra*, 2001].

[32] It is difficult to identify pure signatures of such a dynamical mode using statistical analysis of a highly variable flow, but there is some circumstantial evidence. Analysis of POCM temperature time series at several vertical levels has indicated that there is some vertical coherence in the structure of the 7-month mode (Figure 6). In addition, the 7-month mode in the observations, POCM and the BWBC mode have spatial anomalies with scales of about 500 km which have largest amplitude in the separation region of the Kuroshio. Because the structure near the separation point in the stationary SW-model solution probably looks closer to the real Kuroshio structure than at any other point in the SW-model solution, the real Kuroshio may exhibit variability as occurs in the SW-model solution near the separation point, apart from possible modifications by bottom topography and bottom flow. Also the interpretation by *Kelly et al.* [1996] of the 5–9 month variability in North Pacific observations—a contraction and expansion of the recirculation gyres, which is associated with a large-scale path change—is consistent with the properties of the BWBC mode. However, these signatures cannot be considered as a clear manifestation of the BWBC mode.

[33] From observations and modeling studies, it is known that the Kuroshio has a strong mesoscale activity, which arises through baroclinic instability of the mean flow [*Hurlburt et al.*, 1996]. Typical timescales associated with the variability due to these eddies are about 3 months [*Adamec*, 1998]. As the flow is strongly nonlinear, the interaction of these eddies can easily give a contribution to the 7-month timescale variability, as can variations in atmospheric forcing. Techniques such as M-SSA are all in some way variance maximizing and also pick up these signals. *Nishida and White* [1982] and *Hall* [1991] concluded that barotropic instability conversions play a minimal role in the total variability of the Kuroshio Extension when analyses are done in a natural (stream) coordinate. When the analyses are performed in geographic coordinates, the effect of barotropic instability no longer vanishes, but the variability is still dominated by baroclinic processes. The importance of baroclinic over barotropic energy conversion follows also from the results of *Adamec* [1998, Plate 3], although the use of the *Levitus* [1982] climatology to compute the mean state may blur a correct separation of both contributions. These results also indicate that the relative contributions of barotropic and baroclinic instability conversions depend on the specific frequency, and are not constant in time as well.

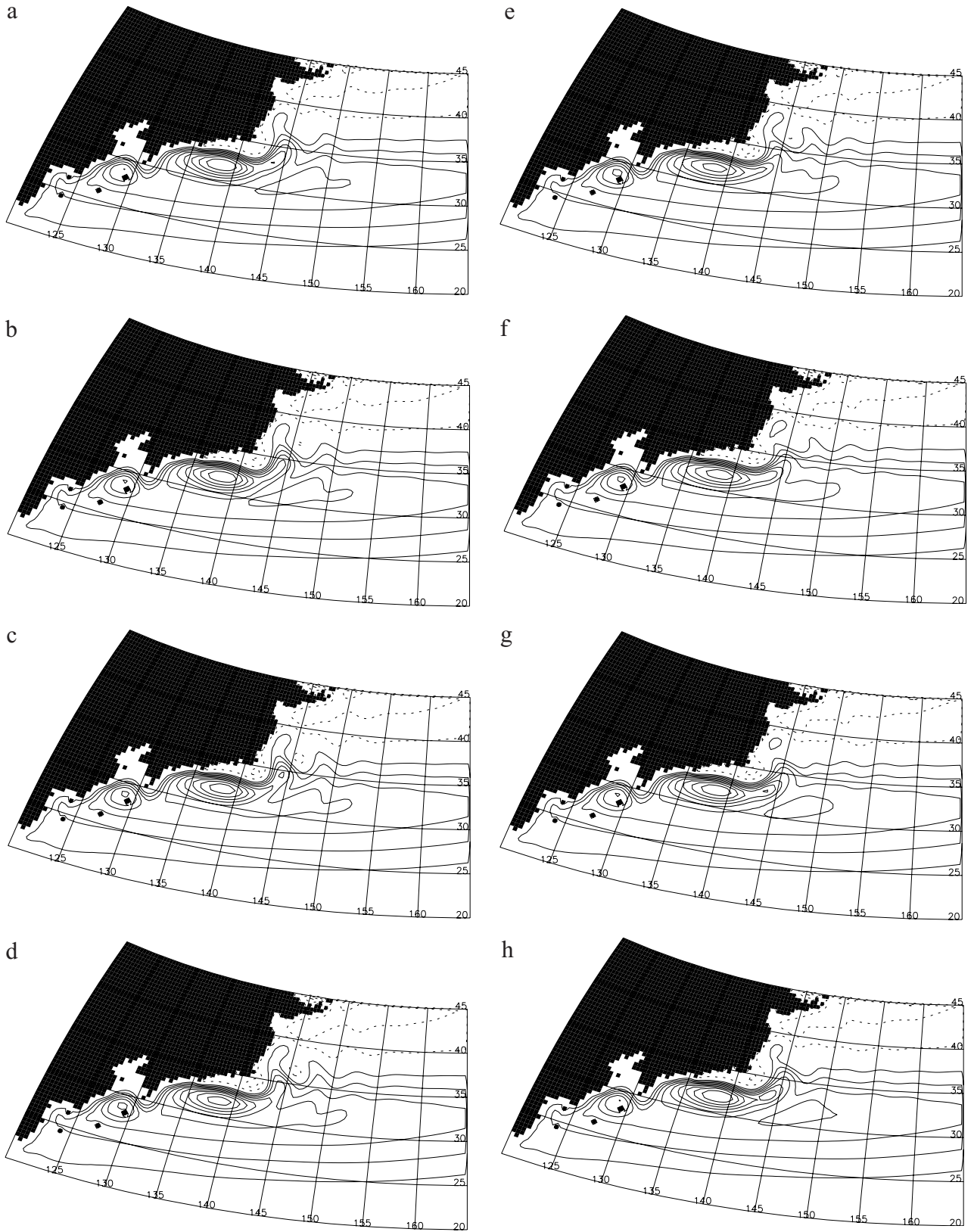


**Figure 11.** Contour plot of SSH deviations for the sum of the steady state and the neutral mode (with an amplitude ratio of 0.2) at the Hopf bifurcation  $H_3$  for  $D = 1044$  m (see also Figure 12a) at several phases of the oscillation and for part of the computational domain  $[120, 165]^\circ\text{E} \times [20, 45]^\circ\text{N}$ : (a)  $\sigma_{it} = 0$ , (b)  $\sigma_{it} = \pi/4$ , (c)  $\sigma_{it} = \pi/2$ , (d)  $\sigma_{it} = 3\pi/4$ , (e)  $\sigma_{it} = \pi$ , (f)  $\sigma_{it} = 5\pi/4$ , (g)  $\sigma_{it} = 3\pi/2$ , and (h)  $\sigma_{it} = 7\pi/4$ .

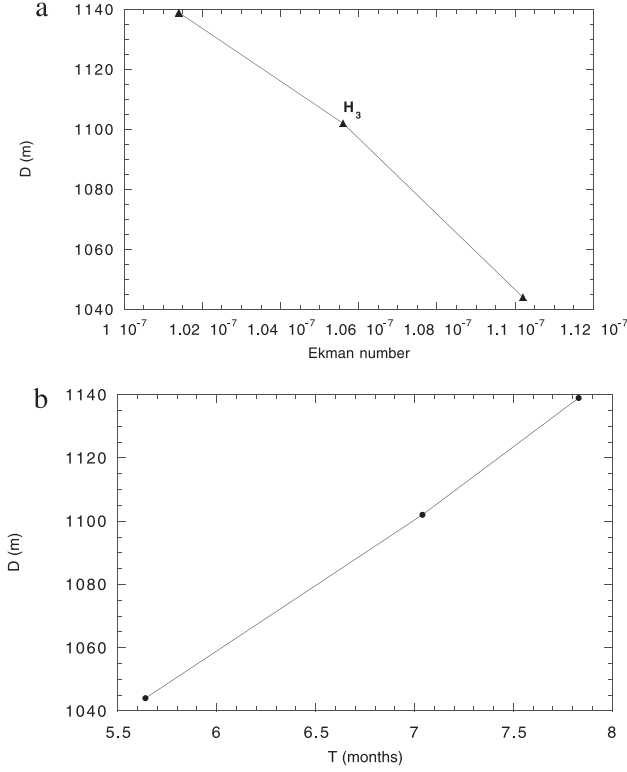


**Figure 12.** (a) Path of the Hopf bifurcation  $H_3$  (see text) in the  $(E, D)$  plane. (b) Oscillation period ( $T$ ) of the neutral mode at  $H_3$  as a function of the layer thickness ( $D$ ).

[34] However, there is no apparent reason why a timescale of 7 months should be preferred in the variability due to the mesoscale eddy field. The fact that the BWBC mode destabilizes the Kuroshio means that this spatial pattern is able to extract energy out of the mean flow on this particular timescale and the energy level of this frequency can be easily increased. Consequently, even if the physics of the variability is not solely caused by the BWBC mode, this mode causes a particular spatiotemporal pattern to be significant because it enhances the variance on this timescale in a totally different way as red noise processes would. The preference at this timescale can hence be viewed as a kind of resonance at 7-month timescale for the nonlinear cascade of energy in the mesoscale eddy field. The differences in the spatial patterns of the 7-month mode in observations and models is therefore likely due to the differences in the structure of the mesoscale fields. The horizontal resolution in POCM is not able to capture all the details of the mesoscale variability and its effects on the mean flow. As a consequence, the time mean path of the Kuroshio has a much smaller extension than in observations and nonlinear interactions of baroclinic eddies will be more localized.

[35] In summary, the strong mesoscale activity in the Kuroshio induces variability with a dominant timescale of about 3 months but, through nonlinear interactions, on many other timescales. If there were only these processes, the Monte Carlo significance test for M-SSA [Allen and Robertson, 1996] would not indicate a longer specific

timescale (i.e. 7 months) as statistically significant. Because there is a preference at this timescale, another source of non-red noise energy must exist. A plausible explanation of this source is the large-scale barotropic instability as found in the shallow-water model. The actual spatiotemporal pattern of the statistical mode would then not only show these barotropic signatures, but also those of the nonlinear interaction patterns due to the mesoscale variability. With this argumentation we conjecture that this specific barotropic instability is involved in the preference for the 7-month variability of the Kuroshio.

## Appendix A: Multichannel Singular Spectrum Analysis (M-SSA)

[36] The technique that we used is M-SSA [Plaut and Vautard, 1994], which produces propagating patterns that are optimal in representing variance. The aim of using M-SSA is to identify coherent space-time patterns, given a regularly sampled archive of maps. M-SSA is mathematically equivalent to extended EOF analysis (EEOF) [Weare and Nassstrom, 1982], but in M-SSA focus is on the temporal structure of the variability, whereas in EEOF the spatial variability is emphasized.

[37] The essentials of the technique are summarized here to introduce terminology used throughout the paper. Let a data set  $\mathbf{X}$  consist of a multichannel time series  $\mathbf{X}_{l,i}$ ,  $i = 1, \dots, N$ ;  $l = 1, \dots, L$ , where  $i$  represents time and  $l$  the channel number. Index  $l$  may represent a point number on a specific grid or a principal component (PC) if the data are prefiltered with principal component analysis (PCA). We assume that  $\mathbf{X}$  has zero mean and is stationary. By making  $M$  lagged copies of  $\mathbf{X}$ , the state vector at time  $i$  is given by

$$(\mathbf{X}_{1,i+1}, \mathbf{X}_{1,i+2}, \dots, \mathbf{X}_{1,i+M}, \mathbf{X}_{2,i+1}, \dots, \mathbf{X}_{2,i+M}, \dots, \mathbf{X}_{L,i+1}, \dots, \mathbf{X}_{L,i+M}). \quad (11)$$

where  $M$  is the window length. The cross-covariance matrix  $\mathbf{T}$  for a chosen window length  $M$  has a general block-Toeplitz form in which each block  $\mathbf{T}_{ll'}$  is the lag covariance matrix (with maximum lag  $M$ ) between channel  $l$  and channel  $l'$ . The  $L \times M$  real eigenvalues  $\lambda_k$  of the symmetric matrix  $\mathbf{T}$  are sorted in decreasing order where an eigenvector (referred to as a ST-EOF)  $\mathbf{E}^k$  is associated with the  $k$ th eigenvalue  $\lambda_k$ . The  $\mathbf{E}^k$  are  $M$ -long time sequences of vectors, describing space-time patterns of decreasing importance as their order  $k$  increases. A space-time principal component (referred to as a ST-PC)  $a^k$  can be computed by projecting  $\mathbf{X}$  onto  $\mathbf{E}^k$ ;  $\lambda_k$  is the variance in  $a^k$ . In this way, the M-SSA expansion of the original data series is given by

$$\mathbf{X}_{l,i+j} = \sum_{k=1}^{L \times M} a_i^k \mathbf{E}_{l,j}^k, j = 1, \dots, M \quad (12)$$

PCA [Preisendorfer, 1988] and single-channel singular spectrum analysis (SSA) [Vautard and Ghil, 1989; Vautard et al., 1992] are particular cases of M-SSA: PCA can be derived from M-SSA with  $M = 1$ , and SSA with  $L = 1$ .

[38] When two consecutive eigenvalues are nearly equal and the two corresponding  $\mathbf{E}^k$  as well as the associated  $a^k$

are in quadrature, then the data possess an oscillation whose period is given by that of  $a^k$  and whose spatial pattern is that of  $\mathbf{E}^k$  [Plaut and Vautard, 1994]. The sum in the right-hand side of equation (12), restricted to one or several terms, describes the part of the signal behaving as the corresponding  $\mathbf{E}^k$ . The components constructed in this way are called reconstructed components (RCs). In this way, the part of the signal involved with an oscillation can be isolated. The original signal is exactly the sum of all the RCs.

[39] As Allen and Robertson [1996] have pointed out, the presence of an eigenvalue pair is not sufficient grounds to conclude that the data exhibits an oscillation. Moreover, low-frequency eigenvalue pairs, which are entirely due to red noise, will appear high in the eigenvalue rank order. A Monte Carlo red noise significance test for M-SSA was therefore constructed [Allen and Robertson, 1996]. This is an objective hypothesis test for the presence of oscillations at low signal-to-noise ratios in multivariate data. Rejection of the red noise null hypothesis using the test should be considered a necessary condition for M-SSA to have detected an oscillation, although in certain situations non-oscillatory processes might also lead to rejection.

[40] The test is built up as follows. Surrogate data segments are constructed by superposing  $L$  uncorrelated AR(1) processes having the same variance and lag-1 autocorrelation as the PCs (from standard PCA) of the data set. Data and surrogate data segments are then projected onto a ST-PC basis of rank  $N - M + 1$ . This basis is either derived from the data cross-covariance (Toeplitz) matrix (referred to as the data adaptive basis) or from the AR(1) process cross-covariance matrix (referred to as the null hypothesis basis). The matrix of projections  $\wedge$  is:

$$\wedge \equiv \mathbf{P}^T \mathbf{Y} \mathbf{Y}^T \mathbf{P} \quad (13)$$

where  $\mathbf{Y}$  is the augmented data matrix of either red noise surrogate data, or the sample time series, and  $\mathbf{P}$  is the ST-PC basis. The method is described in detail by Allen and Robertson [1996].

[41] **Acknowledgments.** This work was supported by the Netherlands Organization for Scientific Research (NWO) under a PIONIER grant to HD. All computations were performed on the CRAY C90 at the Academic Computing Centre (SARA), Amsterdam, the Netherlands, within the project SC498. Use of these computing facilities was sponsored by the National Computing Facilities Foundation with financial support from NWO. The altimeter products have been produced by the CLS Space Oceanography Division (see <http://www.cls.fr>). The authors thank Robin Tokmakian (NPS, USA) for supplying the POCM output, and Andy Robertson (UCLA, USA) for providing the M-SSA software.

## References

Adamec, D., Modulation of the seasonal signal of the Kuroshio Extension during 1994 from satellite data, *J. Geophys. Res.*, *103*, 10,209–10,222, 1998.  
 Allen, M. R., and A. W. Robertson, Distinguishing modulated oscillations from coloured noise in multivariate datasets, *Clim. Dyn.*, *12*, 775–784, 1996.  
 Cronin, M., and D. R. Watts, Eddy-mean flow interaction in the Gulf Stream at 68°W, part I, Eddy energetics, *J. Phys. Oceanogr.*, *26*, 2107–2131, 1996.

Dijkstra, H. A., *Nonlinear Physical Oceanography*, 456 + xviii pp., Kluwer Acad., Norwell, Mass., 2000.  
 Golubitsky, M., and D. Schaeffer, *Singularities and Groups in Bifurcation Theory*, 533 pp., Springer-Verlag, New York, 1985.  
 Hall, M. M., Energetics of the Kuroshio Extension at 35°N, 152°E, *J. Phys. Oceanogr.*, *21*, 958–975, 1991.  
 Hasselmann, K., Stochastic climate models, part I, Theory, *Tellus*, *28*, 473–485, 1976.  
 Hurlburt, H. E., A. J. Wallcraft, W. J. Schmitz, P. J. Hogan, and E. J. Metzger, Dynamics of the Kuroshio/Oyashio current system using eddy-resolving models of the North Pacific Ocean, *J. Geophys. Res.*, *101*, 941–976, 1996.  
 Kawabe, M., Transition processes between the three typical paths of the Kuroshio, *J. Oceanogr. Soc. Jpn.*, *42*, 174–191, 1986.  
 Kelly, K. A., M. J. Caruso, S. Singh, and B. Qiu, Observations of atmosphere-ocean coupling in midlatitude western boundary currents, *J. Geophys. Res.*, *101*, 6295–6312, 1996.  
 Lee, T., and P. Cornillon, Temporal variation of meandering intensity and domain-wide lateral oscillations of the Gulf Stream, *J. Geophys. Res.*, *100*, 13,603–13,613, 1995.  
 Le Traon, P. Y., F. Nadal, and N. Ducet, An improved mapping method of multi-satellite altimeter data, *J. Atmos. Oceanic Technol.*, *25*, 522–534, 1998.  
 Levitus, S., Climatological atlas of the world ocean, *NOAA Prof. Pap.* *13*, 173 pp., U. S. Govt. Print. Off., Washington, D. C., 1982.  
 Nauw, J., and H. A. Dijkstra, The origin of low-frequency variability of double-gyre wind-driven flows, *J. Mar. Res.*, *59*, 567–597, 2001.  
 Nishida, H., and W. B. White, Horizontal eddy fluxes of momentum and kinetic energy in the near-surface of the Kuroshio Extension, *J. Phys. Oceanogr.*, *12*, 160–170, 1982.  
 Plaut, G., and R. Vautard, Spells of low-frequency oscillations and weather regimes in the Northern Hemisphere, *J. Atmos. Sci.*, *51*, 210–236, 1994.  
 Preisendorfer, R. W., *Principal Component Analysis in Meteorology and Oceanography*, Elsevier Sci., New York, 1988.  
 Qiu, B., and T. M. Joyce, Interannual variability in the mid- and low-latitude western North Pacific, *J. Phys. Oceanogr.*, *22*, 1062–1079, 1992.  
 Schmeits, M. J., and H. A. Dijkstra, Physics of the 9-month variability in the Gulf Stream region: Combining data and dynamical systems analyses, *J. Phys. Oceanogr.*, *30*, 1967–1987, 2000.  
 Schmeits, M. J., and H. A. Dijkstra, Bimodal behavior of the Kuroshio and the Gulf Stream, *J. Phys. Oceanogr.*, *31*, 3435–3456, 2001.  
 Semtner, A. J., and R. M. Chervin, Ocean general circulation from a global eddy-resolving model, *J. Geophys. Res.*, *97*, 5493–5550, 1992.  
 Smith, R. D., M. E. Maltrud, F. O. Bryan, and M. W. Hecht, Numerical simulation of the North Atlantic Ocean at  $\frac{1}{10}^\circ$ , *J. Phys. Oceanogr.*, *30*, 1532–1561, 2000.  
 Stammer, D., R. Tokmakian, A. Semtner, and C. Wunsch, How well does a  $1/4^\circ$  global circulation model simulate large-scale oceanic observations?, *J. Geophys. Res.*, *101*, 25,779–25,811, 1996.  
 Taft, B. A., Characteristics of the flow of the Kuroshio south of Japan, in *Kuroshio, Physical Aspects of the Japan Current*, edited by H. Stommel and K. Yoshida, pp. 165–214, Univ. of Wash. Press, Seattle, 1972.  
 Trenberth, K., J. Olson, and W. Large, A global ocean wind stress climatology based on ECMWF analyses, *Tech. Rep. NCARTN-338+STR*, Natl. Cent. for Atmos. Res., Boulder, Colo., 1989.  
 Vautard, R., and M. Ghil, Singular spectrum analysis in nonlinear dynamics with applications to paleoclimatic time series, *Physica D*, *35*, 395–424, 1989.  
 Vautard, R., P. Yiou, and M. Ghil, Singular spectrum analysis: A toolkit for short, noisy chaotic signals, *Physica D*, *58*, 95–126, 1992.  
 Wang, L., C. Kobalinsky, and S. Howden, Annual and intra-annual sea level variability in the region of the Kuroshio Extension from TOPEX/Poseidon and Geosat altimetry, *J. Phys. Oceanogr.*, *28*, 692–711, 1998.  
 Weare, B. C., and J. N. Nasstrom, Examples of extended empirical orthogonal function analyses, *Mon. Weather Rev.*, *110*, 481–485, 1982.

H. Dijkstra, Department of Physics and Astronomy, Institute for Marine and Atmospheric Research Utrecht, Utrecht University, Princetonplein 5, 3584 CC Utrecht, Netherlands. (dijkstra@phys.uu.nl)

M. J. Schmeits, Royal Netherlands Meteorological Institute (KNMI), P.O. Box 201, 3730 AE de Bilt, Netherlands. (schmeits@knmi.nl)